



The Onset and Solidification Path of a Basaltic Melt by *in situ* Differential Scanning Calorimetry (DSC) and *ex situ* Investigations

Letizia Giuliani^{1*}, Gianluca Iezzi^{1,2}, Tyler Hippeli³, Mark Davis³, Aubrey Elbrecht³, Francesco Vetere^{4,5}, Manuela Nazzari² and Silvio Mollo^{2,6}

¹ Dipartimento di Ingegneria e Geologia, Università degli Studi di Chieti-Pescara, Chieti, Italy, ² Istituto Nazionale di Geofisica e Vulcanologia, Rome, Italy, ³ SCHOTT North America, Duryea, PA, United States, ⁴ Dipartimento di Fisica e Geologia, Università degli studi di Perugia, Perugia, Italy, ⁵ Institute of Mineralogy, Leibniz Universität Hannover, Hanover, Germany, ⁶ Dipartimento di Scienze della Terra, Sapienza Università di Roma, Rome, Italy

OPEN ACCESS

Edited by:

Yigang Xu,
Chinese Academy of Sciences, China

Reviewed by:

Huaiwei Ni,
University of Science and Technology
of China, China
Alexandra Yang Yang,
Chinese Academy of Sciences, China

*Correspondence:

Letizia Giuliani
letizia.giuliani@unich.it

Specialty section:

This article was submitted to
Petrology,
a section of the journal
Frontiers in Earth Science

Received: 07 February 2020

Accepted: 20 July 2020

Published: 04 August 2020

Citation:

Giuliani L, Iezzi G, Hippeli T,
Davis M, Elbrecht A, Vetere F,
Nazzari M and Mollo S (2020) The
Onset and Solidification Path of a
Basaltic Melt by *in situ* Differential
Scanning Calorimetry (DSC) and *ex
situ* Investigations.
Front. Earth Sci. 8:337.
doi: 10.3389/feart.2020.00337

The *in situ* differential scanning calorimetry (DSC) technique has been applied to investigate the solidification paths of a basaltic liquid. The starting glass was heated up to 1300°C, kept at this *superliquidus* temperature for 2 h and cooled at rates ($\Delta T/\Delta t$) of 7, 60, 180, 1000, and 1800°C/h, down to 800 and 600°C. Glass transition temperature (T_g), crystallization temperature (T_{x_HR}) and melting temperature (T_m) were measured by *in situ* DSC spectra on heating. T_x measured along the cooling paths (T_{x_CR}) shows exothermic peaks that change from a single symmetric shape (7 and 60°C/h) to multi-component patterns (180, 1000, and 1800°C/h). The recovered products characterized by field emission gun source of the scanning electron microscopy and electron probe micro-analyzer-wavelength dispersive spectrometers show a phase assemblage of spinel (sp), clinopyroxene (cpx), melilite (mel), plagioclase (plg), and glass. Moreover, crystal size distributions (CSDs) and growth rates (G_{max} and G_{CSD}) were also determined. The crystal content slightly increases from 7 to 1800°C/h. Faceted sp are present in all the run products with an amount always <2 area%. Cpx increases from 7 to 1800°C/h, changing its texture from almost faceted to dendritic between 60 and 180°C/h. The area% of mel follows an asymmetric Gaussian trend, while plg nucleates only at 7°C/h with a content <2 area%. The coupling of DSC and SEM outcomes indicate that sp nucleate first, followed by cpx and mel (and/or plg). The increment of $\Delta T/\Delta t$ causes an increase of the CSD slope (m) and crystal population density per size (n_0), as well as a decrease of the crystal size, for both cpx and sp. The log-linear CSD segments with different slopes at 7 and 60°C/h suggest multiple nucleation events and crystal growth by coarsening. G_{max} and G_{CSD} for cpx and sp directly measured on the actual crystallization time by DSC spectra, both increase with the increasing of $\Delta T/\Delta t$. The onset temperature of crystallization (T_{xi}) decreases as $\Delta T/\Delta t$ increases, following an exponential trend that defines the uppermost portion of a time-transformation-temperature-like curve. This analytical model allows us to quantitatively model the kinetic crystallization paths of dry basalts.

Keywords: basalt, DSC, *in situ* crystallization, texture, TTT diagram

INTRODUCTION

Basalts are the most erupted and voluminous products on the Earth surface and their solidification behavior has been the most reproduced process by *ex situ* laboratory experiments. These latter are generally performed starting from *liquidus* or *sub-liquidus* conditions, and quenching the basaltic charges at relative low temperature (T) and/or pressure (P), after different cooling rates ($\Delta T/\Delta t$) (Cashman, 1993; Lasaga, 1998; Hammer, 2008; Iezzi et al., 2009; Del Gaudio et al., 2010; Vetere et al., 2013, 2015; Mollo and Hammer, 2017) and/or decompression rates ($\Delta P/\Delta t$) (Hammer, 2008; Applegarth et al., 2013; Fiege et al., 2015; Mollo and Hammer, 2017; Arzilli et al., 2019). Textural and chemical quantifications of the experimental products make it possible to reconstruct the solidification path of a basaltic system. An alternative *ex situ* approach for investigating nucleation and crystal growth consists of measuring T in basaltic lava flows, sampling the molten portions, and rapidly quenching them in water (Armienti et al., 1994; Burkhard, 2001, 2002, 2003, 2005).

On the other hand, *in situ* investigations are conducted by different approaches, such as: (1) the direct observation with optical microscopy of crystal nucleation and growth (Sunagawa, 1992; Schiavi et al., 2009; Ni et al., 2014), (2) the use of X-ray and neutron scattering measurements or high-resolution X-ray micro-computed tomography (Baker et al., 2013; Arzilli et al., 2015; Zanatta et al., 2017; Polacci et al., 2018; Tripoli et al., 2019), (3) the measurement of viscosity changes during cooling-induced crystallization of basaltic liquids (Vona et al., 2011; Kolzenburg et al., 2016, 2018a,b, 2020; Tripoli et al., 2019), (4) the measurement of electrical conductivity by impedance spectrometry (Xu et al., 2000; Scarlato et al., 2004; Maumus et al., 2005), and (5) the use of differential scanning calorimetry (DSC) and/or differential thermal analysis (DTA). However, the latter methods are more frequently employed in the field of materials science (Dingwell and Webb, 1990; Shelby, 2005; Zheng et al., 2019) rather than in Earth sciences. Particularly, DSC techniques are the most useful and fastest facility to investigate real-time processes occurring during solidification processes (Lange et al., 1994; Burkhard, 2001; Ray et al., 2005, 2010; Castro et al., 2008; Applegarth et al., 2013; Iezzi et al., 2017; Kolzenburg et al., 2020). DSC allows direct measurements of the heat flux released during an exothermic process (e.g., crystallization), and of the heat flux adsorbed during the endothermic ones (e.g., glass transition and melting). As a result, the DSC spectra (T vs $\mu\text{V}/\text{mg}$) resulting from calorimetric solidification experiments show troughs when the glass transitions (T_g) and melting (T_m) occur, and peaks when crystal nucleation and growth start (T_x). However, despite its effectiveness, *in situ* DSC techniques have rarely been used to investigate melting and crystallization processes in basaltic materials (Onorato et al., 1980; Lange et al., 1994; Burkhard, 2001; Ray et al., 2005, 2010; Castro et al., 2008; Applegarth et al., 2013; Iezzi et al., 2017), mainly upon heating (glasses) and to a lesser extent on cooling (melts).

Previous *in situ* investigations conducted on chemically complex (natural) silicate melts (Schiavi et al., 2009; Ni et al., 2014; Kolzenburg et al., 2018a,b) simulated only limited cooling rate ($\Delta T/\Delta t$) conditions and/or restricted thermal ranges of

cooling (ΔT_c). However, natural basaltic liquids solidify under highly variable $\Delta T/\Delta t$ from *liquidus* or *sub-liquidus* regions down to *solidus* temperatures which are still poorly explored (cf. Giuliani et al., 2020a,b) and are important to correctly interpret the thermal interval of crystallization (ΔT_c).

Most of the early experiments on the onset of melt crystallization as a function of cooling rate were not analyzed with scanning electron microscopy (SEM) and/or electron microprobe (EPMA) (Klein et al., 1975; Uhlmann et al., 1975, 1981, 1979; Onorato and Uhlmann, 1976; Onorato et al., 1980), thus preventing quantitative textural and chemical determinations. The only available time-temperature-transformation (TTT) and continuous cooling (CCT) diagrams for basaltic liquids still refer to these pioneering works (Uhlmann et al., 1981; Weinberg and Zanotto, 1989), albeit more recent data have been also reported in literature (Ray et al., 2005; Vetere et al., 2013; Rogez et al., 2017).

In this study, we have combined *in situ* DSC investigations (on heating and especially on cooling) with *ex situ* textural analysis conducted on a basaltic melt cooled from *liquidus* to *solidus* conditions using a broad range of rates of 7, 60, 180, 1000, and 1800°C/h. The SEM analysis on the obtained run products allows the quantification of crystal content (area%), crystals per area (#/A), crystal size distributions (CSDs), and the growth rates of clinopyroxene (cpx) and spinel (sp). The chemical composition of phases was obtained by EPMA-WDS. The *in situ* measurement of the thermal crystallization onset (T_{xi}) leads to analytically model the crystallization paths of basalts, at thermal conditions comparable to those observed for naturally cooling magmas (Vetere et al., 2013, 2015; Giuliani et al., 2020b).

DIFFERENTIAL SCANNING CALORIMETRY

Differential scanning calorimetry is the most common method to investigate the kinetics of solidification, particularly referred to the glass stability (GS) and glass-forming ability (GFA) behaviors (Zheng et al., 2019). Although this, DSC is not so used in Earth Sciences, except few investigations (Onorato et al., 1980; Dingwell and Webb, 1990; Burkhard, 2001; Ray et al., 2005, 2010; Castro et al., 2008; Applegarth et al., 2013; Iezzi et al., 2017; Kolzenburg et al., 2020).

DSC technique allows to quantitatively determine *in situ* the thermodynamic changes occurring during the transformation of a liquid into a solid (cooling) and *vice versa* (heating). These changes are recorded in terms of differential heat flux, measured as DSC/($\mu\text{V}/\text{mg}$), between the analyzed sample and a reference standard (Shelby, 2005). In a typical DSC spectrum, the recorded DSC/($\mu\text{V}/\text{mg}$) is related to T (°C), as shown in **Figures 1, 2A and Supplementary Figure S1**. The endothermic and exothermic peaks result respectively from the heat absorption and release accompanying phase transformations. When the sample reaches the melting point, the recorded heat flux is lower than that of the standard, resulting in the appearance of an endothermic peak that corresponds to the melting temperature (T_m). A similar peak occurs when the sample passes through the glass transition region (T_g). Contrarily, during the crystallization of the sample,

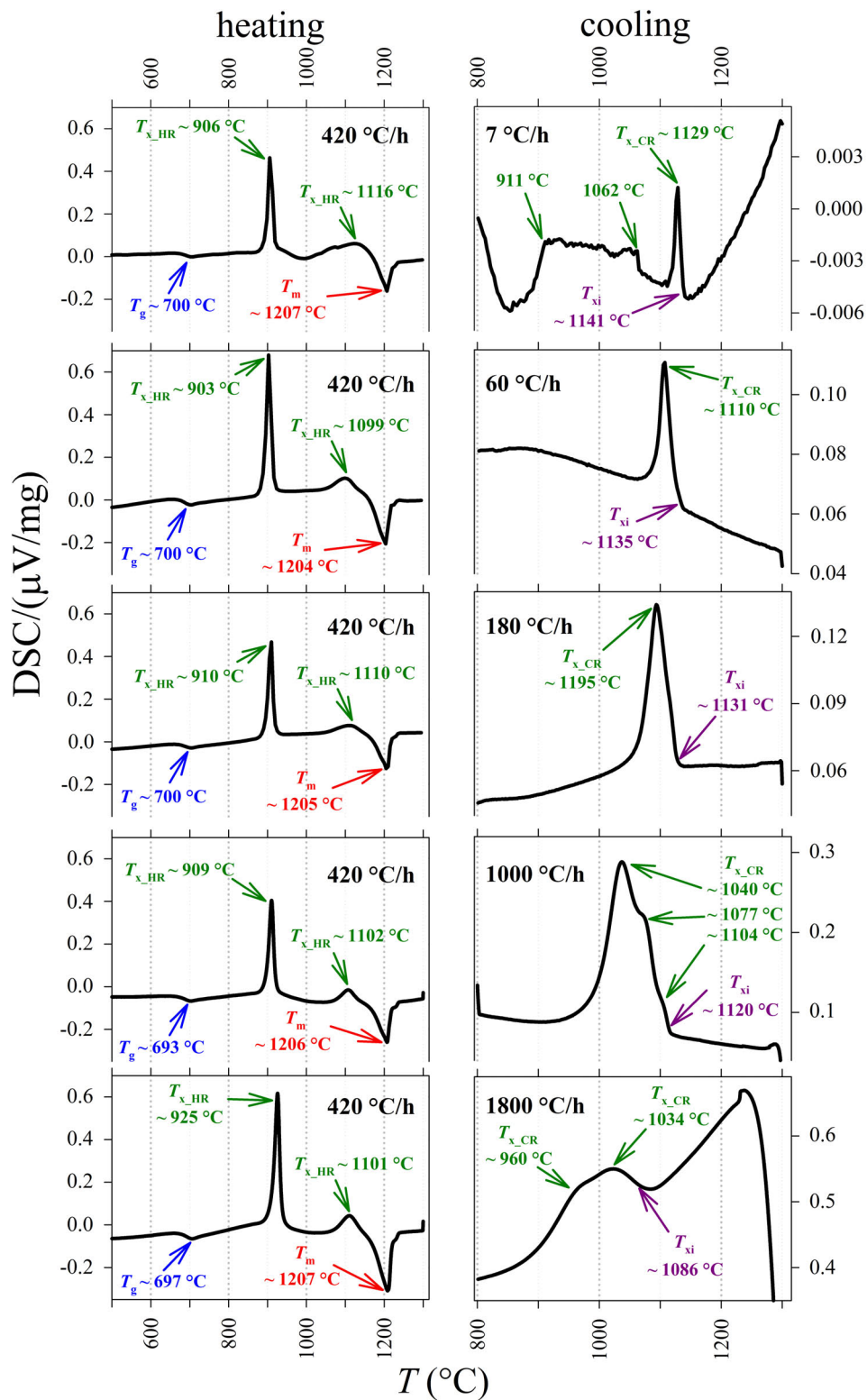
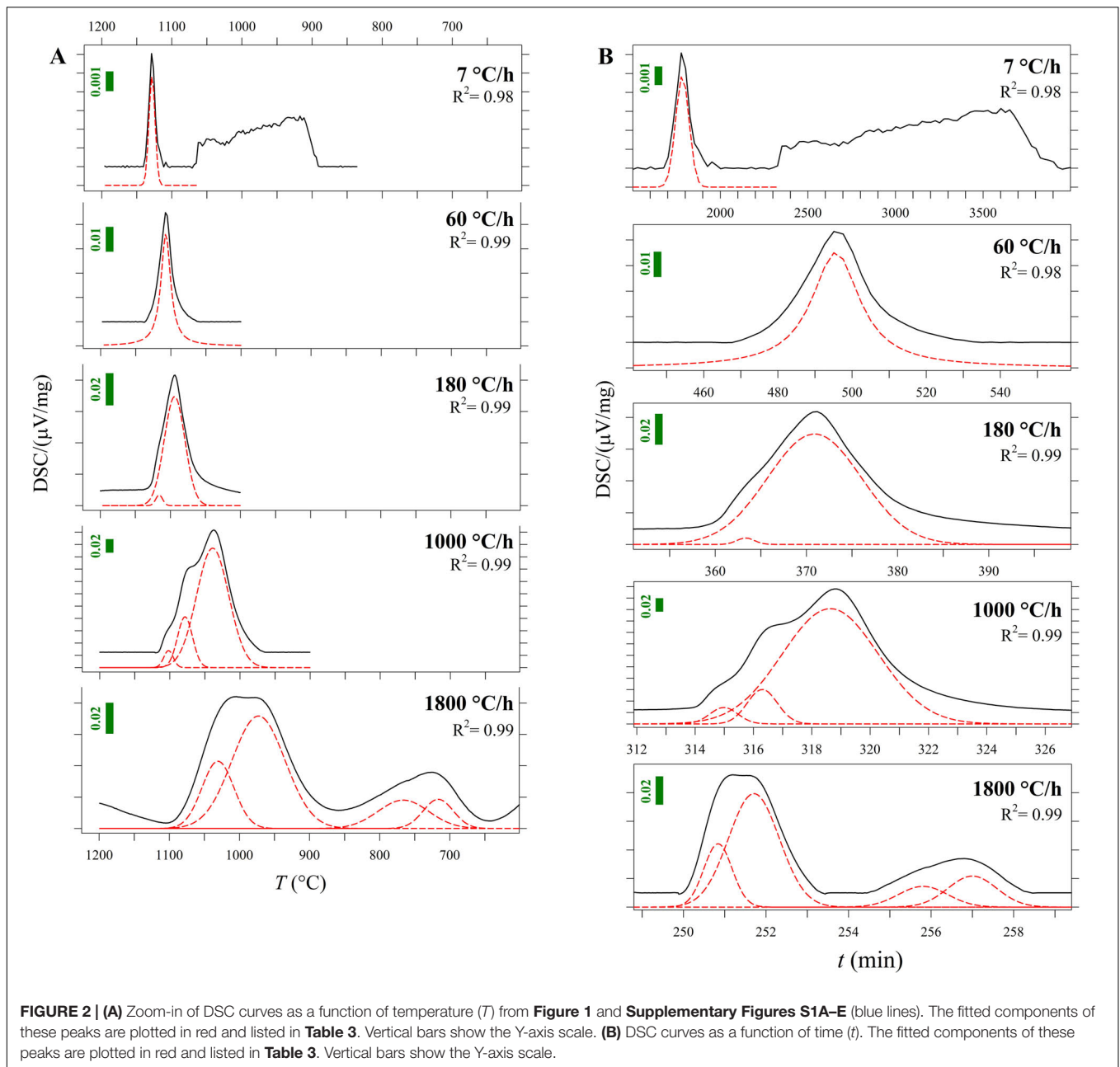


FIGURE 1 | DSC spectra for the basaltic melt, relating the DSC signal based on the differential heat flux (DSC/ $\mu\text{V}/\text{mg}$) and T ($^{\circ}\text{C}$). On the left: heating treatment from ambient temperature to 1300 $^{\circ}\text{C}$ at 420 $^{\circ}\text{C}/\text{h}$. On the right and from top to bottom: cooling rate paths at 7, 60, 180, 1000, and 1800 $^{\circ}\text{C}/\text{h}$, respectively. Glass transition temperature (T_g), crystallization temperature ($T_{x,HR}$) and melting temperature (T_m) were measured by *in situ* DSC spectra acquired on heating. T_x was also measured along the cooling path of the melt ($T_{x,CR}$). The temperature of the onset of crystallization (T_{xi}) has been computed at 10% of the maximum intensity of the crystallization peaks.



the heat flux from the sample is higher than that from the standard, causing the appearance of an exothermic peak on the DSC spectrum at the crystallization temperature (T_x).

In this work, T_m and T_g have been identified during the heating processes, while T_x has been measured both on heating (T_{x_HR}) and along the cooling path (T_{x_CR}).

EXPERIMENTS AND STARTING MATERIAL

A tholeiitic basalt from Iceland (B_{100}) was used to produce a homogeneous starting glass, following the procedure described

in Vetere et al. (2013, 2015). This natural rock is an USGS-international standard known as BIR-1a, which starting composition (wt.%) is: $\text{SiO}_2 = 48.0$; $\text{TiO}_2 = 1.0$; $\text{Al}_2\text{O}_3 = 15.6$; $\text{FeO} = 10.2$; $\text{MnO} = 0.2$; $\text{MgO} = 9.4$; $\text{CaO} = 13.2$; $\text{Na}_2\text{O} = 1.8$; $\text{K}_2\text{O} = 0.0$; $\text{P}_2\text{O}_5 = 0.1$; $\text{H}_2\text{O} = 0.005$.

The B_{100} starting glass was powdered and melted twice at 1600°C for 4 h (ambient P and f_{O_2} of air) and, then, rapidly quenched on a metal plate. For each experiment, several mm-sized B_{100} glass beads were inserted in cylindrical Pt-crucible with a diameter of 6 mm and a length of 4.3 mm. The Pt-charge was lodged in a DSC (Netzsch STA 449F1) installed at the laboratory of SCHOTT Research & Development – North America in Duryea (Pennsylvania, United States) and heated at

a rate of 420°C/h from room temperature to the *superliquidus* conditions of 1300°C (ambient P and f_{O_2} of air; see **Table 1**). The Pt-charges were kept at 1300°C for 2 h and then cooled at rates of 7, 60, 180, 1000, and 1800°C/h down to 800 and 600°C (**Table 1**). The solidification path (heating rate, dwell time, and ΔT_c) used in this study are comparable with those adopted by Vetere et al. (2013, 2015), that applied cooling rates of 1, 7, 60, 180, 1800 and 9000°C/h. The DSC spectra were fitted with a linear background, while the exothermic and endothermic peaks are reproduced using pseudo-Voigt components, such to reproduce the observed spectra and to minimize the difference between measured and calculated DSC patterns.

The recovered run products were mounted in epoxy resin and polished to expose a flat surface. Photomicrographs were collected in the back-scattered electron (BSE) mode, using a field emission gun source of the scanning electron microscopy (FEG-SEM) Jeol 6500F (JEOL, Ltd., Tokyo, Japan). The chemical attributes of phases were determined by an electron probe micro-analyzer (EPMA) Jeol JXA-8200 equipped with five wavelength dispersive spectrometers (WDS). Analyses were performed under vacuum using an electron beam of 5 μm , an accelerating voltage of 15 kV, and an electric current of 7.5 nA. The following standards were adopted: Albite (Na, Si, and Al), Forsterite (Mg), Orthoclase (K), Augite (Fe), Rutile (Ti), Apatite (Ca and P) and Chromite (Cr). Sodium and potassium were analyzed first, to limit their possible migration. Both FEG-SEM and EPMA are installed at the HPHT Laboratory of Experimental Volcanology and Geophysics of the Istituto Nazionale di Geofisica e Vulcanologia (INGV) in Rome, Italy.

The textural features of the run products have been quantified by image analysis on several BSE-SEM micro-photos with magnifications from 100 to 5000 \times (**Table 1**). The image analysis processing is reported in detail in several previous studies (Lanzafame et al., 2013, 2017; Vetere et al., 2013, 2015; Giuliani et al., 2020b); the quantitative textural data are available in the supplementary excel-spreadsheet. The type, size, and distribution of each crystalline phase were measured, plus the CSD analysis. Crystal size distribution curves were calculated using the *CSDcorrections* software (Higgins, 2006; Giuliani et al., 2020b).

RESULTS

DSC Spectra

Differential scanning calorimetry spectra of all the experimental charges are displayed in **Figure 1**; more details and relative

thermal paths are reported in **Supplementary Figures S1A–E**. At the heating rate of 420°C/h it is found (i) a first endothermic peak corresponding to T_g , (ii) two exothermic peaks corresponding to T_{x_HR} , and (iii) a further intense endothermic peak related to the attainment of T_m . T_g occurs between 693 and 700°C, averaging $698 \pm 3^\circ\text{C}$ [i.e., 42°C above the value of 651°C computed by Vetere et al. (2015); **Table 2**]. The first and second peaks of T_{x_HR} are centered between 903 and 925°C (average of $911 \pm 9^\circ\text{C}$) and between 1099 and 1116°C (average of $1104 \pm 7^\circ\text{C}$), respectively (**Table 2** and **Figure 1**). The peaks of T_m vary slightly between 1204 and 1207°C, averaging $1205 \pm 1^\circ\text{C}$ [i.e., 20–25°C and just below the value of 1233°C computed by Vetere et al. (2015); **Table 2** and **Figure 1**].

At *superliquidus* conditions, there are no thermal peaks because the melt is fully relaxed (**Supplementary Figures S1A–E**), whilst one or more exothermic peaks occur at different temperatures as a function of the cooling paths (**Figure 1** and **Supplementary Figures S1A–E**). At $\Delta T/\Delta t$ of 7°C/h, the DSC spectrum shows a first exothermic peak centered at 1129°C, followed by broadband composed of several exothermic peaks between 1062 and 911°C (**Figure 1**). At $\Delta T/\Delta t$ of 60°C/h, a unique asymmetric exothermic peak occurs at 1110°C (**Figure 1**). At $\Delta T/\Delta t$ of 180°C, a slightly asymmetric peak is centered at ca. 1095°C (**Figure 1**), whilst at 1000 and 1800°C/h the corresponding exothermic peaks are broad and composed of several components, which maximum values are in the thermal ranges of 1104–1040°C and 1034–960°C, respectively (**Figure 1**).

To accurately quantify the onset temperature of nucleation under the effect of cooling rate, the first peaks were fitted, as displayed in **Figure 2A**. DSC patterns as a function of time are reported in **Figure 2B**. On cooling, The high- T peaks occurring at $\Delta T/\Delta t$ of 7 and 60°C can be fitted with a single symmetric component, whereas those at $\Delta T/\Delta t$ of 180, 1000 and 1800°C/h are fitted with two, three and four components, respectively (**Figure 2A**); **Table 2** lists these temperatures. The temperature of the onset of crystallization (T_{xi}) has been determined by considering the temperature value at 10% of the maximum intensity of the first peak on cooling and related to crystallization. T_{xi} progressively shifts toward lower values as $\Delta T/\Delta t$ increases (**Figure 1** and **Table 2**). In particular, increasing the $\Delta T/\Delta t$ from 7 to 1800°C/h, decreases the value of T_{xi} from 1141 to 1086°C, as reported in **Table 2**. The difference between averaged T_m and T_{xi} corresponds to the degree of undercooling (ΔT_i), listed in **Table 2**. **Table 3** lists the quantitative attributes of all the fitted components from the DSC spectra.

TABLE 1 | Thermal paths used for *in situ* DSC experiments and BS-SEM microphotographs used for image analysis.

Experimental label	Heating rate (°C/h)	T_i (°C)	Dwell time (h)	$\Delta T/\Delta t$ (°C/h)	T_f (°C)	Experimental time (h)	# Microphotographs for image analysis	Image magnification
DSC-7	420	1300	2	7	800	78.7	5	100 \div 350 \times
DSC-60				60		14.6	3	200 \div 250 \times
DSC-180				180		10.0	5	200 \div 500 \times
DSC-1000				1000		6.6	4	500 \div 1000 \times
DSC-1800				1800	600	5.7	5	1000 \times

TABLE 2 | T_{g-HR} , T_{x-HR} , T_m , T_{x-CR} , T_{xi} , and ΔT_i determined by DSC experiments.

Calculated T_g	T_{g-HR}	Average T_{g-HR}	T_{x-HR}	Average T_{x-HR}	T_m	Average T_m	Calculated T_m	$\Delta T/\Delta t$	T_{x-CR}	T_{xi}	ΔT_i
651	700	698 (± 3)	906–1116	911 (± 9)– 1104 (± 7)	1207	1206 (± 1)	1233	7	1129–1062/911	1141	65
	700		903–1099		1204			60	1110	1135	71
	700		910–1100		1205			180	1095	1131	75
	693		909–1102		1206			1000	1104–1040–1077	1120	86
	697		925–1101		1207			1800	1034–960	1086	120

All data are in °C, except $\Delta T/\Delta t$ in °C/h. Calculated values of T_g and T_m are reported in Vetere et al. (2015). Glass transition temperature (T_g), crystallization temperature (T_{x-HR}), and melting temperature (T_m) were measured by in situ DSC spectra acquired on heating. T_x was also measured along the cooling path of the melt (T_{x-CR}), while T_x has been measured at 10% of the maximum intensity of the first crystallization peak. The degree of undercooling (ΔT_i) was calculated as T_m average – T_{xi} .

TABLE 3 | Data from DSC spectra and calculated crystallization time.

$\Delta T/\Delta t$ (°C/h)	Peak	T vs. $\mu V/mg$				t vs. $\mu V/mg$				Time of crystallization (min)
		Center (°C)	FWHM	% area	Area	Center (min)	FWHM	% area	Area	
7	1	921	38	21.5	0.08	1784	90	15.2	0.56	2300
	2	978	90	53.4	0.21	2478	229	6.8	0.25	
	3	1048	27	8.5	0.03	3100	793	54.1	2.00	
	4	1128	10	16.6	0.06	3582	358	23.8	0.88	
	Total				100	0.39			100	
60	1	1107	17	100	1.2	496	16	100	1.11	57.5
	Total			100	1.2			100	1.11	
180	1	1094	35	96.8	2.56	363	2	1.1	0.01	26.5
	2	1116	12	3.2	0.08	371	12	98.9	0.89	
	Total			100	2.64			100	0.90	
1000	1	1039	54	80.6	11.16	315	1	3.6	0.03	8.9
	2	1078	25	16.0	2.22	316	1	8.3	0.08	
	3	1101	16	3.4	0.47	319	4	88.1	0.83	
	Total			100	13.84			100	0.94	
1800	1	716	50	8.39	1.00	251	1	17.7	0.03	8.9
	2	766	85	13.7	1.63	252	1	45.6	0.09	
	3	973	89	57.2	6.81	256	2	14.9	0.03	
	4	1031	54	20.6	2.46	257	1	21.8	0.04	
	Total			100	11.90			100	0.19	

Individual peaks were fitted by pseudo-Voigt approximation with peak energy and full width at half maximum (FWHM) as seed values.

Texture and Crystal-Chemistry

Figure 3 displays the textural features of the solidified DSC charges. These products contain crystals of spinel (sp), clinopyroxene (cpx), melilite (mel) and/or plagioclase (only at 7°C/h), and glass. Sp crystals display always equant and faceted, hopper shapes. Conversely, cpx at $\Delta T/\Delta t$ of 7°C/h are almost faceted and prismatic, frequently attaching on sp or pre-existing cpx crystals (**Figure 3**), while cpx obtained at $\Delta T/\Delta t \geq 60^\circ\text{C/h}$ show dendritic forms with fern-like elongated shapes. Mel crystallizes with either elongated H-shapes or razor blade-like aspects (**Figure 3**).

Figure 4 and **Table 4** report the quantitative abundance of phases. The amount of sp comprises a very low area% of between 0.1 and 1.9, while that of cpx increases from 32.1 to 47.3 area% as $\Delta T/\Delta t$ increases from 7 to 1800°C/h. The abundance of mel is also limited and changes from 5.3 to 8.9 and finally to 1.9 area%, following a broad and asymmetric Gaussian-like trend. Plg occurs only at $\Delta T/\Delta t$ of 7°C/h with an amount of 1.7 area%. Overall the whole glass content monotonically decreases with increasing

$\Delta T/\Delta t$ (**Table 4**), reflecting the slight increase of the total crystal content (**Figure 4** and **Table 4**).

The analyses of chemical attributes of phases are reported in **Figure 5** and **Supplementary Table S1**. As the $\Delta T/\Delta t$ increases, all the major oxides of cpx, mel, and glass approach those of the starting composition. In particular, cpx records an increase in SiO₂, Al₂O₃, and Na₂O contents, and a decrease in MgO and CaO, while FeO remains almost constant. Intra-crystalline glass follows the opposite trends of cpx, whereas those of sp are limited (**Figure 5**). The relatively highest (>10 wt.%) chemical variations are recorded for mel: indeed, as the $\Delta T/\Delta t$ augments, SiO₂ increases, and both FeO + MgO decrease, whilst Na₂O + CaO are almost constant; Al₂O₃ follows an irregular decreasing trend (**Figure 5**).

DISCUSSION

Phase relations and crystal contents from our DSC experiments can be conveniently compared with those from previous *ex situ*

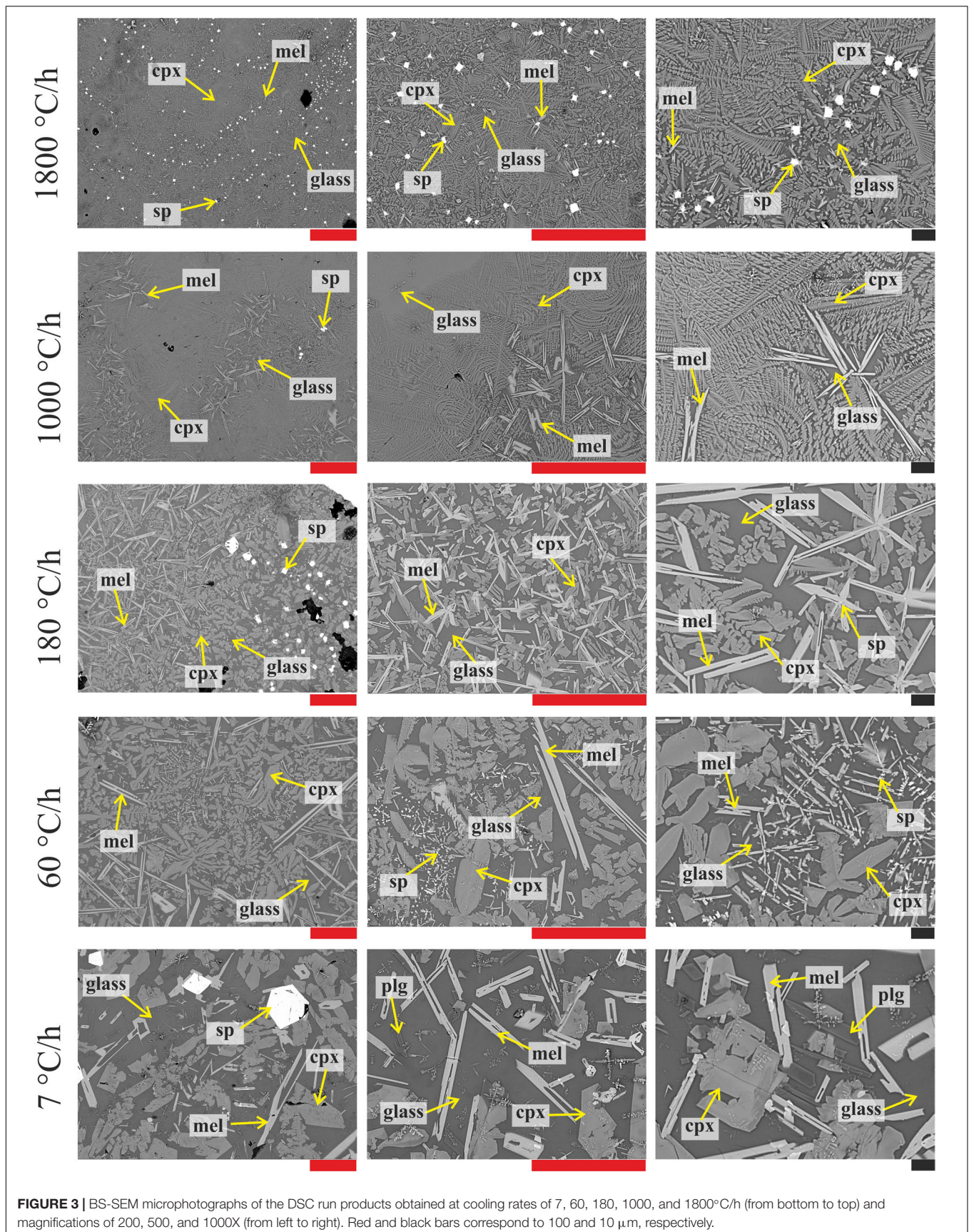
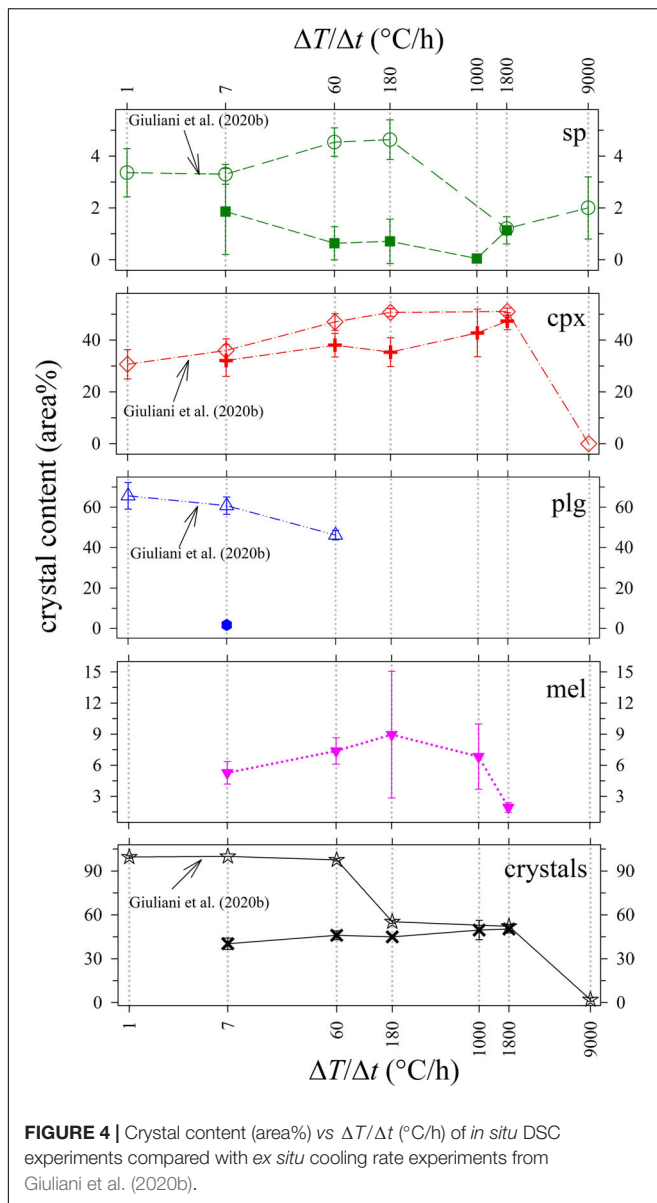


FIGURE 3 | BS-SEM microphotographs of the DSC run products obtained at cooling rates of 7, 60, 180, 1000, and 1800°C/h (from bottom to top) and magnifications of 200, 500, and 1000X (from left to right). Red and black bars correspond to 100 and 10 μm, respectively.

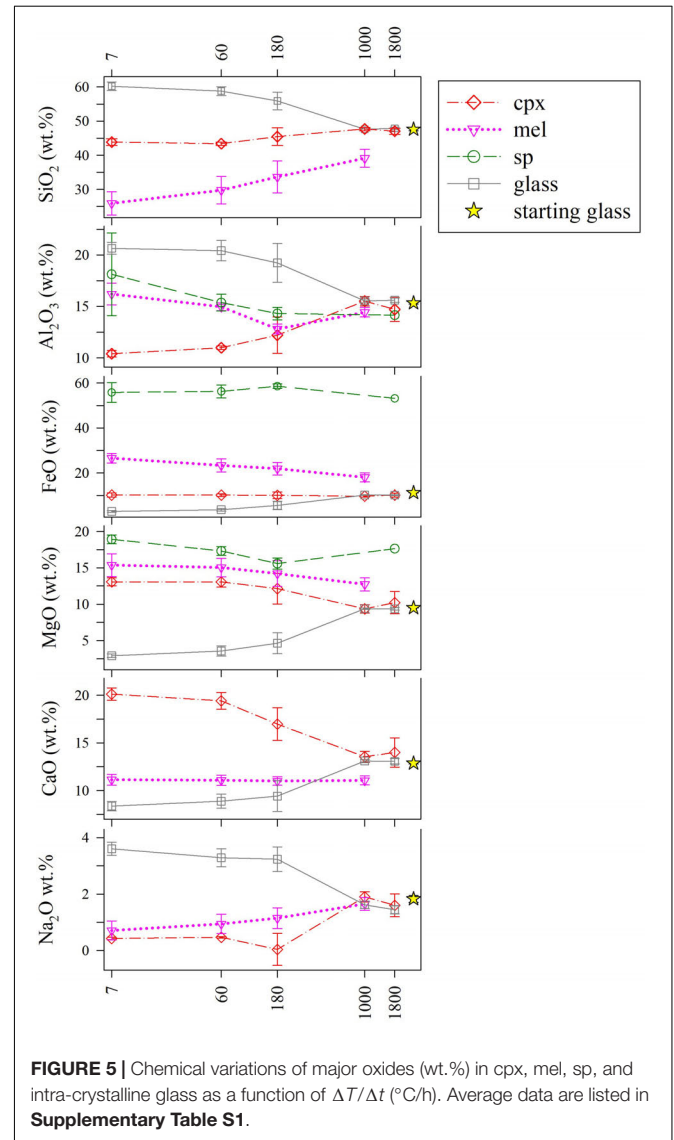


cooling rate experiments conducted by Vetere et al. (2013, 2015) and further analyzed by Giuliani et al. (2020b), run at similar solidification conditions. As shown in **Figure 4**, the amount of sp in the DSC run products is low (0–2 area%), and comparable with 2–5 area% content quantified by Giuliani et al. (2020b). Also, the amount of cpx in DSC run products increases with increasing $\Delta T/\Delta t$ in a similar manner to that observed in Giuliani et al. (2020b). The cpx contents at $\Delta T/\Delta t$ of 7 and 1800 $^{\circ}\text{C}/\text{h}$ are practically identical, whilst those at $\Delta T/\Delta t$ of 60 and 180 $^{\circ}\text{C}/\text{h}$ differ by 5 and 10 area%, respectively (**Figure 4**). Therefore, the crystallization of sp and cpx is well comparable with the *ex situ* dynamic experiments run in furnaces.

By contrast, in DSC run products, mel is <10 area%, and plg is low to absent (**Table 4** and **Figure 4**). The different amount of plg between the DSC experiments and those reported in Vetere

TABLE 4 | Phase proportions (area%); standard deviations in parenthesis.

$\Delta T/\Delta t$ ($^{\circ}\text{C}/\text{h}$)	Glass	sp	cpx	plg	mel	Crystals
7	59.7 (3.9)	1.9 (1.7)	32.1 (6.1)	1.7 (0.7)	5.3 (1.1)	38.2 (6.7)
60	53.9 (3.0)	0.6 (0.6)	38.0 (4.5)	–	7.3 (1.3)	44.8 (3.6)
180	55.0 (1.5)	0.7 (0.9)	35.3(5.6)	–	8.9 (6.1)	46.2 (3.4)
1000	50.4 (6.6)	0.1 (0.1)	42.7 (9.2)	–	6.8 (3.1)	49.6 (6.6)
1800	49.7 (2.7)	1.1 (0.5)	47.3 (3.3)	–	1.9 (0.5)	50.3 (2.7)



et al. (2015) and Giuliani et al. (2020b) can be interpreted in the frame of the TTT diagrams (Lasaga, 1998; Shelby, 2005; Wang et al., 2012; Vetere et al., 2013). In a TTT diagram (t vs. T), the nucleation rate (I), the degree of undercooling (ΔT), and the time required to initiate nucleation of a crystalline phase (τ or induction time) are strictly related (Lasaga, 1998; Fokin et al., 2003, 2008; Roskosz et al., 2005; Iezzi et al., 2009). At the apex of the TTT curve, the nucleation rate is strongly variable and has its maximum value (I_{max}), while τ is

minimum. For the basaltic composition investigated here, the ΔT is moderate at temperatures of 1000–1100°C (Vetere et al., 2013). When a $\Delta T/\Delta t$ trajectory is close to I_{\max} , even small thermal (fluctuations and/or gradient) and/or mechanical (flowing and/or deformation) perturbations can produce significant changes of the nucleation of crystalline phases and their rate (Kirkpatrick, 1983; Vetere et al., 2013).

We hypothesize that during *in situ* DSC experiments the temperature oscillations were extremely low or even absent, indeed lower than those experienced by charges run by Vetere et al. (2013, 2015). This resulted in unfavorable conditions for the crystallization of a SiO₂- and tetrahedral connected-rich crystal, like plg. Indeed, extremely stable thermal and/or mechanical conditions favor the metastable nucleation of mel, a sorosilicate with lower SiO₂ amount, and poorly connected tetrahedra. It is a note of worth that mel solidified also in the B₁₀₀ experimental charges solidified *ex situ* at $\Delta T/\Delta t > 60^\circ\text{C/h}$, by Vetere et al. (2013, 2015), although with a smaller content. These considerations attest that the plg phase is stable only at low $\Delta T/\Delta t$, where kinetics conditions are moderate to low, in agreement with Lange et al. (1994), and is more reluctant to nucleate than mel (Kirkpatrick, 1983; Vetere et al., 2015). Thereby, mel oversteps plg due to its lower SiO₂ content and degree of polymerization (Kirkpatrick, 1983; Lasaga, 1998; Zhang et al., 2003; Iezzi et al., 2009, 2014). On these bases, the common presence of plg in natural tholeiitic rocks could be also related to the presence of thermal and mechanical perturbations (Chakraborty, 1995; Lasaga, 1998; Vetere et al., 2013), while the rarity of mel in basaltic rocks (Deer et al., 1992) is due to the relatively high SiO₂ content of these magmas and the inevitable presence of thermal and mechanical perturbations. All these hypotheses are corroborated by recent findings by Tripoli et al. (2019) and Kolzenburg et al. (2020) on the role of mechanical

perturbations on nucleation in solidifying basaltic liquids. They reported that flowing and stress on solidifying basaltic melts promote gradients in chemical potential, enhance the diffusion rates, and, consequently, increasing the crystallization (nucleation and growth) rates and reduced the incubation time. This also favors the kinetic crystallization of metastable phases, rather than the thermodynamically favored ones (Tripoli et al., 2019).

Thereby, we suggest that in the DSC facility used in this study, contrarily to those observed in Giuliani et al. (2020b), the thermal and/or mechanical fluctuations were extremely low or even absent, disfavoring the chemical diffusion of elements. Such conditions did not favor the nucleation of plg, especially at moderate to high cooling conditions. In turn, mel nucleated under *disequilibrium* condition. Noteworthy, poor tetrahedral-connected cpx phases crystallized in the DSC apparatus and in Giuliani et al. (2020b) with similar behaviors (Figure 4).

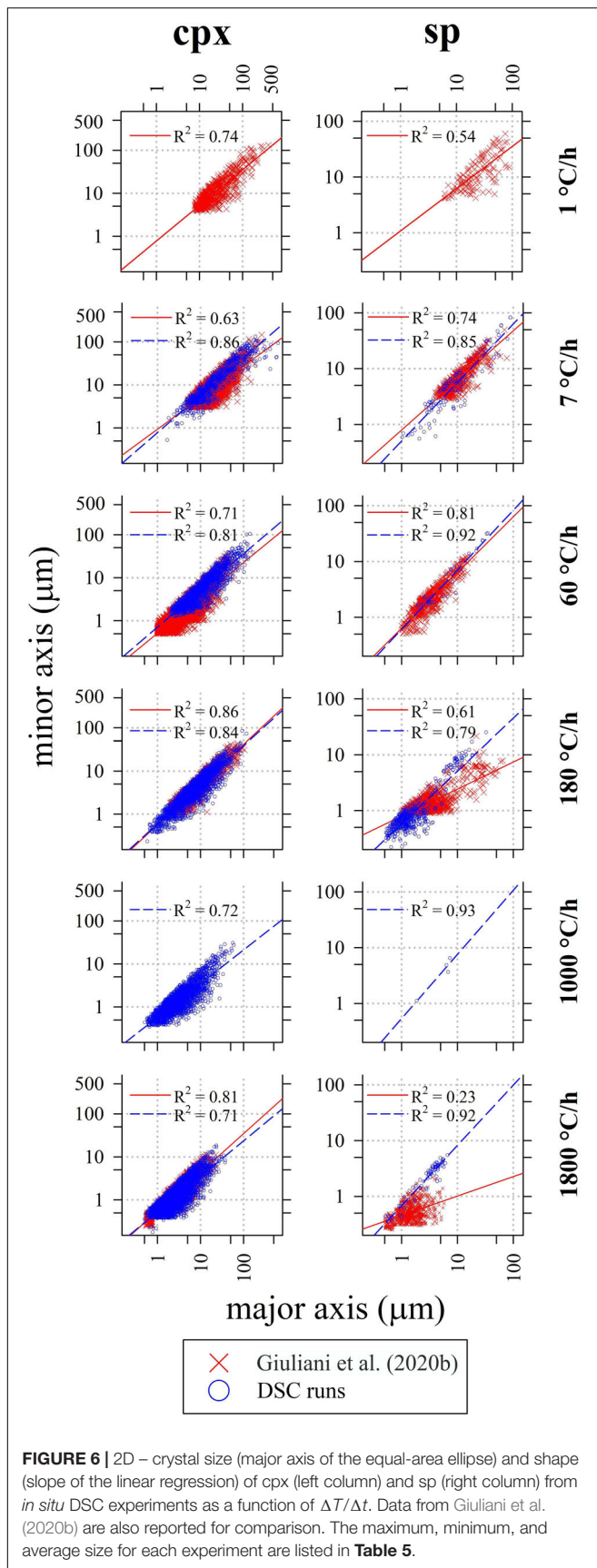
Moreover, DSC experiments at $\Delta T/\Delta t$ of 1000 and 1800°C/h indicate also that cpx heterogeneously nucleates on sp, whereas mel develops around cpx-rich areas (Figure 3). Owing on these textural and chemical outcomes, the crystallization sequence in the analyzed basaltic composition is sp, cpx, mel, and \pm plg, in line with the interpretation of Vetere et al. (2015) and Giuliani et al. (2020b). This also agrees with the observation that the oxide amounts of mel and glass are anti-correlated (Figure 5); hence mel metastably crystallizes in the melt left behind the growth of sp and cpx. Finally, being the mel amount in the DSC charges very low (<10 area%, Table 4), sp and cpx highly reproducible, the representativeness of these DSC experimental outcomes is reliable, especially at high T below the *liquidus*.

The crystal sizes of cpx, sp, and mel decrease as a function of $\Delta T/\Delta t$ (Table 5). As $\Delta T/\Delta t$ increases from 7 to 1800°C/h, the measured crystal size range decreases from 635–2 to 38–1 μm ,

TABLE 5 | 2D maximum (L_{\max}), minimum (L_{\min}) and averaged (L_{av}) crystal lengths, CSDs parameters (m and n_0), maximum (G_{\max}) and average (G_{CSD}) growth rates.

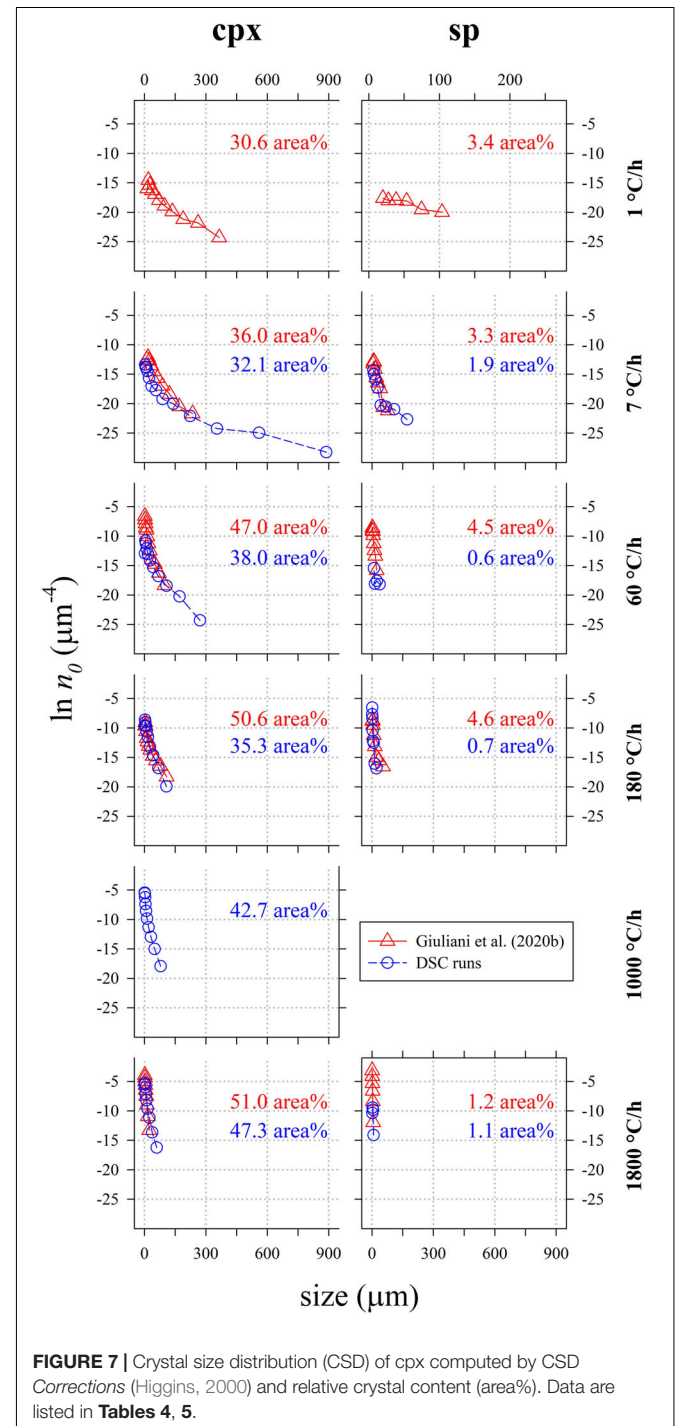
$\Delta T/\Delta t$ ($^\circ\text{C/h}$)	Crystalline phase	L_{\max} (μm)	L_{\min} (μm)	L_{av} (μm)	m (μm^{-1})	$\ln(n_0)$ (μm^{-4})	(n_0) (μm^{-4})	G_{\max} (cm/s)	G_{CSD} (cm/s)
7	cpx	635	2	41	-3×10^{-2}	-14.8	4×10^{-7}	4×10^{-7}	2×10^{-8}
	sp	89	1	15	-6×10^{-2}	-14.7	4×10^{-7}	5×10^{-8}	1×10^{-8}
	mel	359	1	24	-5×10^{-2}	-13.9	1×10^{-6}	1×10^{-7}	2×10^{-8}
60	cpx	165	2	16	-7×10^{-2}	-11.5	1×10^{-5}	4×10^{-6}	4×10^{-7}
	sp	35	2	10	-1×10^{-1}	-14.6	4×10^{-7}	9×10^{-7}	3×10^{-7}
	mel	259	2	24	-2×10^{-1}	-11.0	2×10^{-5}	6×10^{-6}	2×10^{-7}
180	cpx	117	1	11	-1×10^{-1}	-8.9	1×10^{-4}	6×10^{-6}	5×10^{-7}
	sp	33	1	2	-8×10^{-1}	-5.8	3×10^{-3}	1×10^{-6}	7×10^{-8}
	mel	145	1	13	-9×10^{-2}	-10.5	3×10^{-5}	6×10^{-6}	7×10^{-7}
1000	cpx	59	1	5	-2×10^{-1}	-6.0	3×10^{-3}	1×10^{-5}	8×10^{-7}
	sp	7	2	6	-	-	-	1×10^{-6}	-
	mel	44	1	10	-1×10^{-1}	-9.3	1×10^{-4}	8×10^{-6}	1×10^{-6}
1800	cpx	38	1	4	-3×10^{-1}	-5.2	5×10^{-3}	6×10^{-6}	7×10^{-7}
	sp	7	1	3	-2×10^{-1}	-8.8	2×10^{-4}	1×10^{-6}	9×10^{-7}
	mel	14	1	3	-3×10^{-1}	-6.7	1×10^{-3}	2×10^{-6}	6×10^{-7}

G values are obtained as $G_{\max} = L_{\max}/t$ and $G_{\text{CSD}} = -1/mt$ (Zieg and Marsh, 2002). L_{\max} is the average of the maximum lengths of five longest crystals, m is the average CSD slope, and t is the time of crystallization. In Giuliani et al. (2020b), t was computed considering the time needed to cool the starting composition from 1233 (T_m) to 800°C (T_f). For the DSC run products, t has been directly measured on the crystallization peaks (Figure 2B), considering the crystallization time intervals reported in Table 3, i.e., 1677–1927 min (7°C/h), 498–525 min (60°C/h), 358–385 min (180°C/h), 314–323 min (1000°C/h), 250–259 min (1800°C/h).



from 89-1 to 7-1 μm , and from 359-1 to 14-1 μm for cpx, sp, and mel, respectively (**Table 5**). Notably, the crystal sizes measured for sp and cpx from *in situ* DSC experiments are also comparable to those quantified by *ex situ* cooling rate experiments analyzed by Giuliani et al. (2020b) (**Figure 6**).

Crystal size distribution curves of cpx and sp are displayed in **Figure 7** and compared with those reported in Giuliani et al. (2020b). These curves allow to make three-dimensional



consideration about textures: they are computed using the 2D crystal sizes (maximum and minor axis), image area (μm^2), crystal shape and phase abundances (area%); the stereological conversions are implemented in the software used to compute the CSDs (Higgins, 2006). Results show that with increasing $\Delta T/\Delta t$, the slope (m) and crystal population density per size (n_0 , corresponding to the y -axis intercept) of cpx-CSD trajectories increase (Figure 7 and Table 5). These data well match with those reported in Giuliani et al. (2020b) for $\Delta T/\Delta t$ of 180 and $1800^\circ\text{C}/\text{h}$. Conversely, CSDs compared at $\Delta T/\Delta t$ of 7 and $60^\circ\text{C}/\text{h}$ show lower crystal sizes for the experimental charges analyzed by Giuliani et al. (2020b) due to the significant crystallization of plg. CSD curves obtained for sp from DSC experiments do not show a clear evolutionary trend as a function of $\Delta T/\Delta t$ and they poorly match with data from Giuliani et al. (2020b) (Figure 7). Overall, cpx- and sp-CSD curves on the run-product cooled in the DSC at $\Delta T/\Delta t$ of 7 show both two log-linear segments with different slopes (Figure 7), accounting for multiple nucleation events and subsequent crystal growth by coarsening. The minimum slope corresponding to a maximum crystal size relates to the first nucleation event, further nucleation pulses at lower temperatures follow (Pupier et al., 2008; Giuliani et al., 2020b).

The other CSDs instead show a nearly unique log-linear evolution (Figure 7).

These considerations agree with the very rapid crystallization, on the order of minutes, measured *in situ* by Polacci et al. (2018) using X-ray tomography. They rapidly cooled a natural basalt from 1250°C (*superliquidus* condition) to 1170 and 1150°C (low to moderate ΔT), maintaining the final temperature for 4 h. During the annealing at 1150 and 1170°C , it is possible to identify at least three discrete nucleation events for sp and cpx. Also, Polacci et al. (2018) observed the heterogeneous crystallization of cpx on sp. Similarly, DSC spectra from this study display discrete exothermic peaks of crystallization (Figure 1 and Supplementary Figures S1B–E), except for the charges at $7^\circ\text{C}/\text{h}$, showing a complex and broad DSC multicomponent band at a relatively low thermal range (911 – 1062°C), that suggests the attainment of a continuous crystallization process (Figure 1 and Supplementary Figure S1A). In line with this, a long tail at large crystal sizes ($>300 \mu\text{m}$) along with low m and n_0 values (Figure 7) characterize the CSD curve of this experiment. Possibly, the exothermic multicomponent band and the long CSD tail observed at $\Delta T/\Delta t$ of $7^\circ\text{C}/\text{h}$ are both determined by crystal coarsening phenomena. It is thus possible to assume that nucleation occurs mainly by a rapid pulse during cooling and

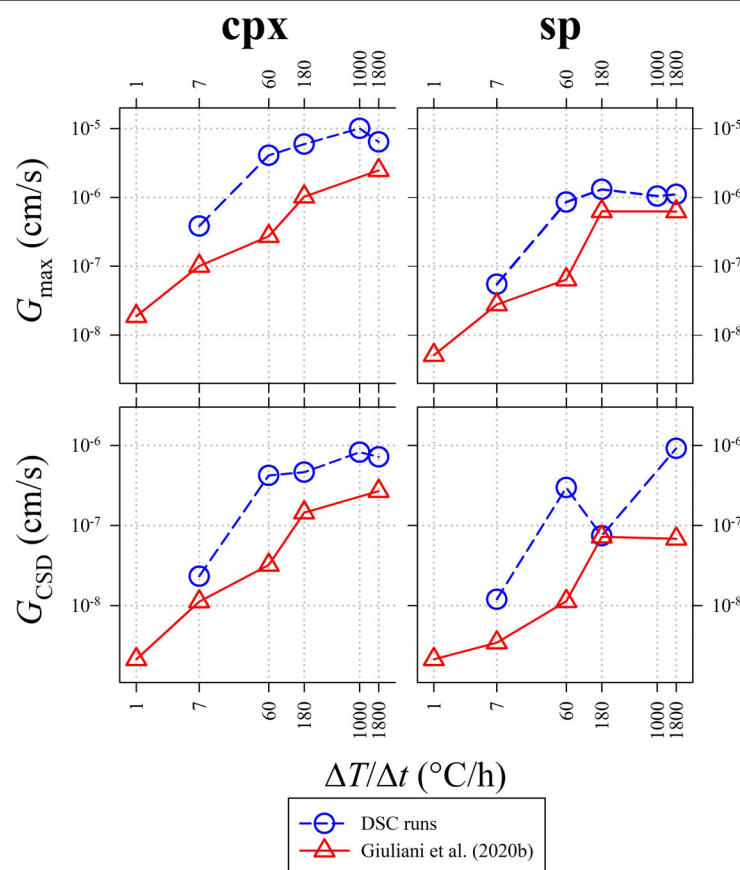
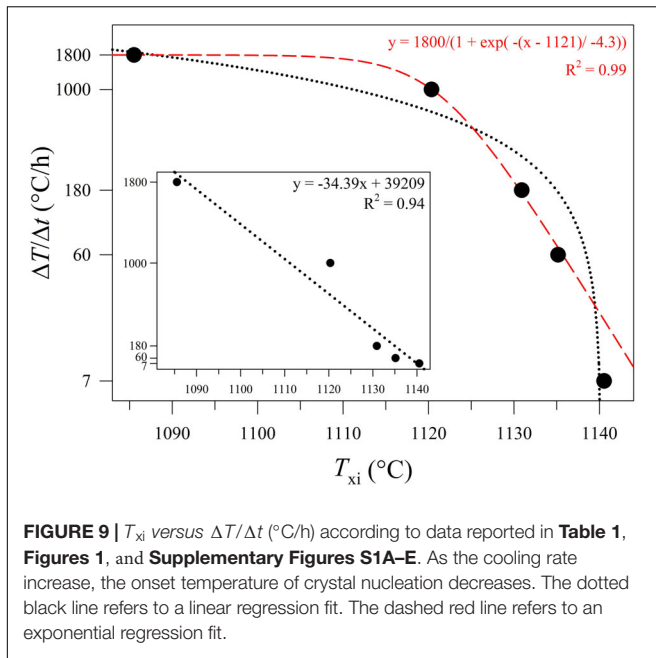


FIGURE 8 | Variation of the maximum growth rate (G_{max} ; top) and the average CSD growth rate (G_{CSD} ; bottom). Data from DSC experiments (Table 5) are compared with those reported in Giuliani et al. (2020b).

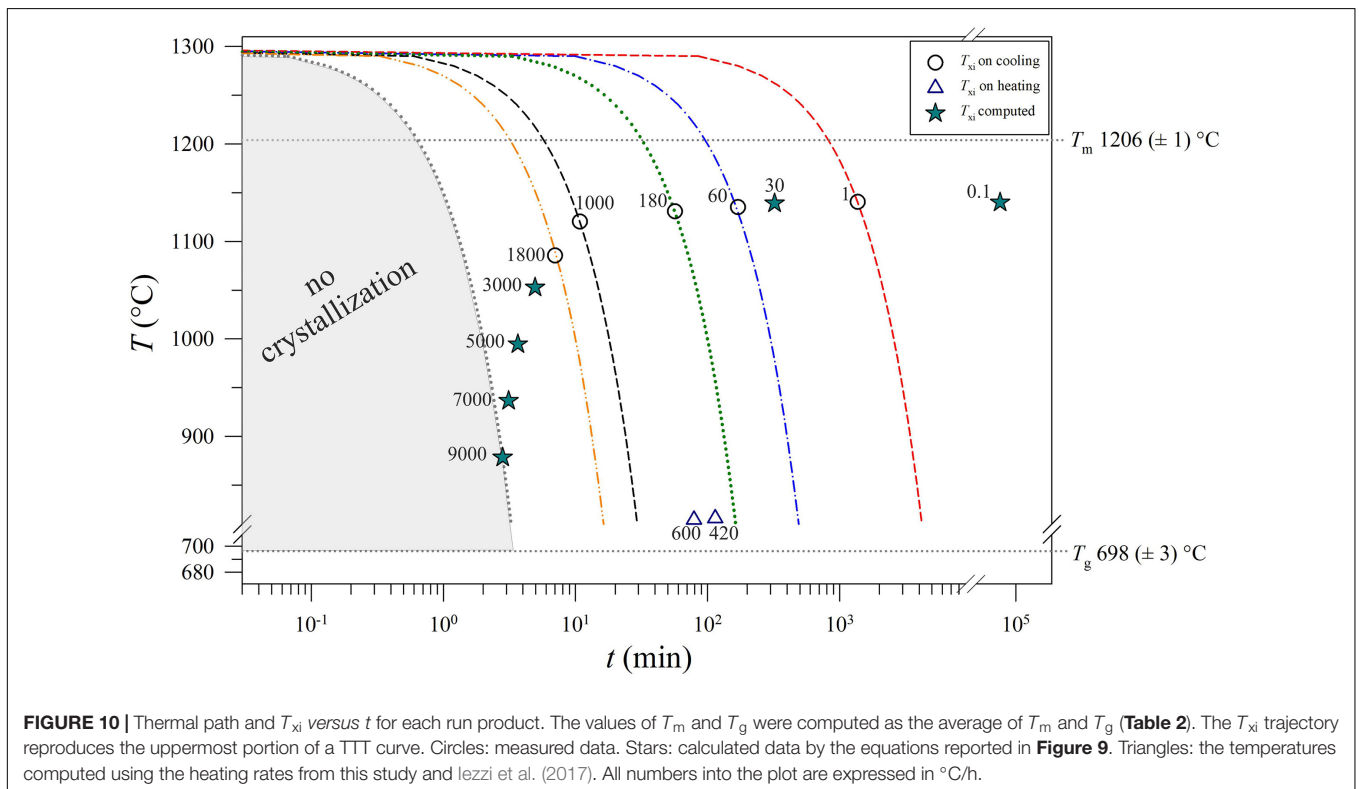


that mainly, at low rates, crystal coarsening becomes a dominant solidification process.

Calculation of the maximum growth rate (G_{\max}) uses the maximum lengths (L_{\max}) of five longest crystals (Burkhard, 2002; Hammer and Rutherford, 2002; Couch, 2003; Iezzi et al., 2011;

Giuliani et al., 2020b). In particular, the average L_{\max} has been divided by the actual crystallization time (t) measured from the DSC spectra (**Figures 1, 2B** and **Table 3**). The average growth rate (G_{CSD}) has been also determined by interpolating m (**Table 5**) with t , as $G_{\text{CSD}} = -1/mt$ (Zieg and Marsh, 2002; Giuliani et al., 2020b). The values of G_{\max} and G_{CSD} from this study are reported in **Table 5** and plotted in **Figure 8**, together with the G_{\max} and G_{CSD} from Giuliani et al. (2020b). Both the G s of cpx and sp obtained from DSC experiments are systematically higher than those measured by *ex situ* cooling rate experiments (**Figure 8**), due to a more accurate and reliable estimate of t from DSC spectra (**Figures 1, 2B** and **Table 3**). Generally, G_{\max} and G_{CSD} increase as a function of $\Delta T/\Delta t$, with the only exception of G_{CSD} of sp derived at $\Delta T/\Delta t$ between 60 and $180^{\circ}\text{C}/\text{h}$ (**Figure 8**).

The values of T_{xi} (**Table 2**) vs. $\Delta T/\Delta t$ are reported in **Figure 9**, showing a decreasing exponential evolution that highlights the faster decrease of T_{xi} at higher kinetic conditions, with respect to low $\Delta T/\Delta t$. Results of data fitted using linear regression a high correlation too. Importantly, these experimental data and the fitting exponential equation have been used to reconstruct the uppermost portion of a TTT curve of the basaltic melt solidifying at ambient conditions (**Figure 10**). According to Vetere et al. (2015), a cooling rate of $9000^{\circ}\text{C}/\text{h}$ prevents the crystallization (crystals < 2 area%) of a basaltic liquid. Since dynamic stress conditions in volcanic systems enhance the nucleation process (Kouchi et al., 1986; Vona and Romano, 2013; Kolzenburg et al., 2018a,b, 2020; Vetere et al., 2020), the TTT data from this study represent the conservative expression of a kinetic crystallization process governed by cooling rate.



CONCLUSION

We present a complete and quantitative characterization of a basaltic melt solidifying from *liquidus* to *solidus* conditions, monitored *in situ* via DSC heating/cooling experiments, able to track the thermal evolution and crystallization path of the system. Direct measurement of the onset temperature of crystallization makes possible to define the nucleation and growth processes in an interval of 911–1129°C, at atmospheric pressure and fugacity of air. Textural analysis of cpx and sp shows that both m and n_0 of CSDs increase with increasing $\Delta T/\Delta t$, while the crystal size ranges decrease. These data point out that the sp nucleation favors those of cpx; at the slow kinetic condition, cpx formation happens by multiple nucleation events, followed by crystal coarsening.

The T_{xi} depicts a decreasing exponential trend as a function of cooling rate; under low kinetic conditions, the onset of nucleation starts after a long time at high temperature (low ΔT), as expected from theory. The T_{xi} values measured and/or computed using the founded analytical function define the uppermost part of a TTT-like trend, making it possible to quantitatively model the crystallization path of a basaltic melt solidifying at ambient conditions.

DATA AVAILABILITY STATEMENT

All datasets generated for this study are included in the article/**Supplementary Material**.

AUTHOR CONTRIBUTIONS

LG acquired BS-SEM images, performed the image analysis and, together with GI, organized the data in tables and

figures, and wrote an early version of the manuscript. GI conceived the study. TH, MD, and AE carried out the DSC experiments. MN contributed to the BS-SEM acquisition. All the authors discussed together the data and their interpretation, as well as contributed to the attainment of this final version.

FUNDING

This study was funded by the “Fondi Ateneo of the University G. D’Annunzio”, PRIN (2009PZ47NA_003) project “Experimental determination of the glass-forming ability (GFA), nucleation and crystallization of natural silicate melts” and PRIN (2017J277S9_003) project “Time scales of solidification in magmas: Application to Volcanic Eruptions, Silicate Melts, Glasses, Glass-Ceramics” awarded to GI. Alexander von Humboldt foundation senior research grant to FV is also acknowledged.

ACKNOWLEDGMENTS

The authors thank the editor YX and the two reviewers. Most of this study was conducted during the Ph.D. of LG.

SUPPLEMENTARY MATERIAL

The Supplementary Material for this article can be found online at: <https://www.frontiersin.org/articles/10.3389/feart.2020.00337/full#supplementary-material>

REFERENCES

- Applegarth, L. J., Tuffen, H., James, M. R., and Pinkerton, H. (2013). Degassing-driven crystallisation in basalts. *Earth Sci. Rev.* 116, 1–16. doi: 10.1016/j.earscirev.2012.10.007
- Armienti, P., Pareschi, M. T., Innocenti, F., and Pompilio, M. (1994). Effect of magma storage and ascent on kinetics of crystal growth. *Contrib. Mineral. Petrol.* 115, 402–414. doi: 10.1007/bf00320974
- Arzilli, F., Agostini, C., Landi, P., Fortunati, A., Mancini, L., and Carroll, M. R. (2015). Plagioclase nucleation and growth kinetics in a hydrous basaltic melt by decompression experiments. *Contrib. Mineral. Petrol.* 170:55. doi: 10.1007/s00410-015-1205-1209
- Arzilli, F., La Spina, G., Burton, M. R., Polacci, M., Le Gall, N., Hartley, M. E., et al. (2019). Magma fragmentation in highly explosive basaltic eruptions induced by rapid crystallization. *Nat. Geosci.* 12, 1023–1028. doi: 10.1038/s41561-019-0468-466
- Baker, D. R., Brun, F., O’Shaughnessy, C., Mancini, L., Fife, J. L., and Rivers, M. (2013). A four-dimensional X-Ray tomographic microscopy study of bubble growth in basaltic foam. *Nat. Commun.* 3:1135. doi: 10.1038/ncomms2134
- Burkhard, D. J. (2003). Thermal interaction between lava lobes. *Bull. Volvanol.* 65, 136–143. doi: 10.1007/s00445-002-0249-247
- Burkhard, D. J. (2005). Nucleation and growth rates of pyroxene, plagioclase and Fe-Ti oxides in basalt under atmospheric conditions. *Eur. J. Mineral.* 17, 675–685. doi: 10.1127/0935-1221/2005/0017-0675
- Burkhard, D. J. M. (2001). Crystallization and oxidation of Kilauea basalt glass: processes during reheating experiments. *J. Petrol.* 42, 507–527. doi: 10.1093/ptetrology/42.3.507
- Burkhard, D. J. M. (2002). Kinetics of crystallization: example of micro-crystallization in basalt lava. *Contrib. Mineral. Petrol.* 142, 724–737. doi: 10.1007/s00410-001-0321-x
- Cashman, K. V. (1993). Relationship between plagioclase crystallization and cooling rate in basaltic melts. *Contrib. Mineral. Petrol.* 113, 126–142. doi: 10.1007/bf00320836
- Castro, J. M., Beck, P., Tuffen, H., Nichols, A. R. L., Dingwell, B., and Martin, M. C. (2008). Timescales of spherulite crystallization in obsidian inferred from water concentration profiles. *Am. Min.* 93, 1816–1822. doi: 10.2138/am.2008.2904
- Chakraborty, S. (1995). “Diffusion in silicate melts,” in *Structure And Dynamics Of Silicate Melts. Review in Mineralogy and Geochemistry*, eds J. F. Stebbins, D. B. Dingwell, and P. W. McMillan, (Cham: Springer), 441–497.
- Couch, S. (2003). Experimental investigation of crystallization kinetics in a haplogranite system. *Am. Min.* 88, 1471–1485. doi: 10.2138/am-2003-1011
- Deer, W. A., Howie, R. A., and Zussman, J. (1992). *An Introduction To The Rock-Forming Minerals*. Upper Saddle River, NJ: Prentice Hall.
- Del Gaudio, P., Mollo, S., Ventura, G., Tezzi, G., Taddeucci, J., and Cavallo, A. (2010). Cooling rate-induced differentiation in anhydrous and hydrous basalts at 500 MPa: implications for the storage and transport of magmas in dykes. *Chem. Geol.* 270, 164–178. doi: 10.1016/j.chemgeo.2009.11.014
- Dingwell, D. B., and Webb, S. L. (1990). Relaxation in silicate melts. *Eur. J. Mineral.* 2, 427–449.

- Fiege, A., Vetere, F., Iezzi, G., Simon, A., and Holtz, F. (2015). The roles of decompression rate and volatiles ($H_2O + Cl \pm CO_2 \pm S$) on crystallization in (trachy-) basaltic magma. *Chem. Geol.* 411, 310–322. doi: 10.1016/j.chemgeo.2015.07.016
- Fokin, V. M., Yuritsyn, N. S., Zanutto, E. D., Schmelzer, J. W. P., and Cabral, A. A. (2008). Nucleation time-lag from nucleation and growth experiments in deeply undercooled glass-forming liquids. *J. Non Cryst. Solids* 354, 3785–3792. doi: 10.1016/j.jnoncrysol.2008.05.011
- Fokin, V. M., Zanutto, E. D., and Schmelzer, J. W. P. (2003). Homogeneous nucleation versus glass transition temperature of silicate glasses. *J. Non Cryst. Solids* 321, 52–65. doi: 10.1016/S0022-3093(03)00089-9
- Giuliani, L., Iezzi, G., and Mollo, S. (2020a). Dynamics of volcanic systems: physical and chemical models applied to equilibrium versus disequilibrium solidification of magmas. *AGU Books* 16, 373–418.
- Giuliani, L., Iezzi, G., Vetere, F., Behrens, H., Mollo, S., Cauti, F., et al. (2020b). Evolution of textures, crystal size distributions and growth rates of plagioclase, clinopyroxene and spinel solidified at variable cooling rates from a mid-ocean ridge basaltic liquid. *Earth Sci. Rev.* 204:103165. doi: 10.1016/j.earscirev.2020.103165
- Hammer, J. E. (2008). “Experimental studies of the kinetics and energetics of magma crystallization,” in *Minerals, Inclusions and Volcanic Processes. Reviews in Mineralogy and Geochemistry*, eds K. D. Putirka, and F. J. Tepley, (Washington, DC: Mineralogical Society of America and Geochemical Society), 9–59. doi: 10.2138/rmg.2008.69.2
- Hammer, J. E., and Rutherford, M. J. (2002). An experimental study of the kinetics of decompression-induced crystallization in silicic melt. *J. Geophys. Res.* 107:2021.
- Higgins, M. D. (2000). Measurement of crystal size distributions. *Am. Min.* 85, 1105–1116. doi: 10.2138/am-2000-8-901
- Higgins, M. D. (2006). *Quantitative Textural Measurement In Igneous And Metamorphic Petrology*. Cambridge: Cambridge University Press.
- Iezzi, G., Elbrecht, A. L., Davis, M., Vetere, F., Misiti, V., Mollo, S., et al. (2017). Glass Stability (GS) of chemically complex (natural) sub-alkaline glasses. *J. Non Cryst. Solids* 477, 21–30. doi: 10.1016/j.jnoncrysol.2017.09.047
- Iezzi, G., Mollo, S., Shaini, E., Cavallo, A., and Scarlato, P. (2014). The cooling kinetics of plagioclase revealed by electron microprobe mapping. *Am. Min.* 99, 898–907. doi: 10.2138/am.2014.4626
- Iezzi, G., Mollo, S., Torresi, G., Ventura, G., Cavallo, A., and Scarlato, P. (2011). Experimental solidification of an andesitic melt by cooling. *Chem. Geol.* 283, 261–273. doi: 10.1016/j.chemgeo.2011.01.024
- Iezzi, G., Mollo, S., and Ventura, G. (2009). “Solidification behavior of natural silicate melts and volcanological implications,” in *Volcanoes: Formation, Eruptions And Modeling*, eds N. Lewis, and A. Moretti, (New York, NY: Nova publishers), 127–151.
- Kirkpatrick, R. J. (1983). Theory of nucleation in silicate melts. *Am. Min.* 68, 66–77.
- Klein, L., Onorato, P. I. K., Uhlmann, D. R., and Hopper, R. W. (1975). Viscous flow, crystallization behavior and thermal histories of lunar breccias 70019 and 79155. *Proc. Lunar. Sci. Conf.* 4, 579–593.
- Kolzenburg, S., Di Genova, D., Giordano, D., Hess, K. U., and Dingwell, D. B. (2018a). The effect of oxygen fugacity on the rheological evolution of crystallizing basaltic melts. *Earth Planet. Sci. Lett.* 487, 21–32. doi: 10.1016/j.epsl.2018.01.023
- Kolzenburg, S., Giordano, D., Hess, K. U., and Dingwell, D. B. (2018b). Shear rate-dependent disequilibrium rheology and dynamics of basalt solidification. *Geophys. Res. Lett.* 45, 6466–6475. doi: 10.1029/2018GL077799
- Kolzenburg, S., Giordano, D., Cimarelli, C., and Dingwell, D. B. (2016). In-situ thermal characterization of cooling/crystallizing lavas during rheology measurements and implications for lava flow emplacement. *Geochim. Cosmochim. Acta* 195, 244–258. doi: 10.1016/j.gca.2016.09.022
- Kolzenburg, S., Hess, K. U., and Dingwell, D. B. (2020). Disequilibrium rheology and crystallization kinetics of basalts and implications for the Phlegrean volcanic District. *Front. Earth Sci.* 8:187. doi: 10.3389/feart.2020.00187
- Kouchi, A., Tsuchiyama, A., and Sunagawa, I. (1986). Effect of stirring on crystallization kinetics of basalt: texture and element partitioning. *Contrib. Min. Petrol.* 93, 429–438. doi: 10.1007/bf00371713
- Lange, R. A., Cashman, K. V., and Navrotsky, A. (1994). Direct measurements of latent heat during crystallization and melting of a ugandite and an olivine basalt. *Contrib. Min. Petrol.* 118, 169–181. doi: 10.1007/bf01052867
- Lanzafame, G., Iezzi, G., Mancini, L., Lezzi, F., Mollo, S., and Ferlito, C. (2017). Solidification and turbulence (non-laminar) during magma ascent: insights from 2D and 3D analyses of bubbles and minerals in an Etnean dyke. *J. Petrol.* 58, 1511–1534. doi: 10.1093/ptrology/egx063
- Lanzafame, G., Mollo, S., Iezzi, G., Ferlito, C., and Ventura, G. (2013). Unravelling the solidification path of a *pahoehoe* “cicirara” lava from Mount Etna volcano. *Bull. Volc.* 75–4, 1–16. doi: 10.1007/s00445-013-0703-708
- Lasaga, A. C. (1998). *Kinetic theory in the Earth Sciences*. New York, NY: Princeton university press.
- Maumus, J., Bagdassarov, N., and Schmelting, H. (2005). Electrical conductivity and partial melting of mafic rocks under pressure. *Geochim. Cosmochim. Acta* 69, 4703–4718. doi: 10.1016/j.gca.2005.05.010
- Mollo, S., and Hammer, J. E. (2017). “Dynamic crystallization in magmas,” in *Mineral Reaction Kinetics: Microstructures, Textures, Chemical And Isotopic Signatures. EMU Notes in Mineralogy*, eds W. Heinrich, and R. Abart, (McLean: European Mineralogical Union), 1–46. doi: 10.1180/EMU-notes.16.12
- Ni, H., Keppler, H., Walte, N., Schiavi, F., Chen, Y., Masotta, M., et al. (2014). In-situ observation of crystal growth in a basalt melt and development of crystal size distribution in igneous rocks. *Contrib. Mineral. Petrol.* 167:1003. doi: 10.1007/s00410-014-1003-9
- Onorato, P. I. K., and Uhlmann, D. R. (1976). Nucleating heterogeneities and glass formation. *J. Non Cryst. Solids* 22, 367–378. doi: 10.1016/0022-3093(76)90066-1
- Onorato, P. I. K., Uhlmann, D. R., and Hopper, R. W. (1980). A kinetic treatment of glass formation: IV. Crystallization on reheating a glass. *J. Non Cryst. Solids* 41, 189–200. doi: 10.1016/0022-3093(80)90164-7
- Polacci, M., Arzilli, F., La Spina, G., Le Gall, N., Cai, B., Hartley, M. E., et al. (2018). Crystallization in basaltic magmas revealed via in situ 4D synchrotron X-ray microtomography. *Sci. Rep.* 8:8377. doi: 10.1038/s41598-018-26644-26646
- Pupier, E., Duchene, S., and Toplis, M. J. (2008). Experimental quantification of plagioclase crystal size distribution during cooling of a basaltic liquid. *Contrib. Mineral. Petrol.* 155, 555–570. doi: 10.1007/s00410-007-0258-259
- Ray, C. S., Reis, S. T., Brow, R. K., Höland, W., and Rheinberger, V. (2005). A new DTA method for measuring critical cooling rate for glass formation. *J. Non Cryst. Solids* 351, 1350–1358. doi: 10.1016/j.jnoncrysol.2005.03.029
- Ray, C. S., Reis, S. T., Sen, S., and O’Dell, J. S. (2010). JSC-1A lunar soil simulant: characterization, glass formation, and selected glass properties. *J. Non Cryst. Solids* 356, 2369–2374. doi: 10.1016/j.jnoncrysol.2010.04.049
- Rogez, J., Papin, S., Benigni, P., and Jousseume, C. (2017). “Thermodynamic of the glassy and crystalline states-general kinetic to return to equilibrium,” in *From Glass To Crystals. Nucleation, Growth And Phase Separation, From Research To Applications*, eds D. R. Neuville, L. Cormier, D. Caurant, and L. Montagne, (France: EDP Sciences).
- Roskosz, M., Toplis, M. J., and Richet, P. (2005). Experimental determination of crystal growth rates in highly supercooled aluminosilicate liquids. *Implic. Rate Control. Process. Am. Min.* 90, 1146–1156. doi: 10.2138/am.2005.1627
- Scarlato, P., Poe, B. T., and Freda, C. (2004). High-pressure and high-temperature measurements of electrical conductivity in basaltic rocks from Mount Etna, Sicily, Italy. *J. Geophys. Res.* 109:B02210. doi: 10.1029/2003JB002666
- Schiavi, F., Walte, N., and Keppler, H. (2009). First in-situ observation of crystallization processes in a basaltic-andesitic melt with the moissanite cell. *Geology* 37, 963–966. doi: 10.1130/G30087A.1
- Shelby, J. E. (2005). *Introduction To Glass Science And Technology*, 2nd Edn, Padstow: Conwall.
- Sunagawa, I. (1992). In situ investigation of nucleation, growth and dissolution of silicate crystals at high temperatures. *Annu. Rev. Earth. Planet. Sci.* 20, 113–142. doi: 10.1146/annurev.ea.20.050192.000553
- Tripoli, B., Manga, M., Mayeux, J., and Barnard, H. (2019). The effects of deformation on the early crystallization kinetics of basaltic magmas. *Front. Earth. Sci.* 7:250. doi: 10.3389/feart.2019.00250
- Uhlmann, D. R., Klein, L., Onorato, P. I. K., and Hopper, R. W. (1975). The formation of lunar breccias: sintering and crystallization kinetics. *Proc. Lunar Sci. Conf.* 45, 693–705.
- Uhlmann, D. R., Klein, L., Onorato, P. I. K., and Scherer, G. W. (1979). “A simplified model for glass formation,” in *Proceedings of the Lunar and Planetary Science Conference*, New York, NY.

- Uhlmann, D. R., Yinnon, H., and Fang, C. H. (1981). "Simplified model evaluation of cooling rates for glass-containing lunar composition," in *Proceedings of the Lunar and Planetary Science Conference*, Houston, TX.
- Vetere, F., Iezzi, G., Behrens, H., Cavallo, A., Misiti, V., Dietrich, M., et al. (2013). Intrinsic solidification behavior of basaltic to rhyolitic melts: a cooling rate experimental study. *Chem. Geol.* 354, 233–242. doi: 10.1016/j.chemgeo.2013.06.007
- Vetere, F., Iezzi, G., Behrens, H., Holtz, F., Ventura, G., Misiti, V., et al. (2015). Glass forming ability and crystallization behavior of sub-alkaline silicate melts. *Earth Sci. Rev.* 150, 25–44. doi: 10.1016/j.earscirev.2015.07.001
- Vetere, F., Mazzeo, A., Perugini, D., and Holtz, F. (2020). Viscosity behaviour of silicate melts during cooling under variable shear rates. *J. Non Cryst. Solids* 477, 21–30.
- Vona, A., and Romano, C. (2013). The effect of undercooling and deformation rates on the crystallization kinetics of Stromboli and Etna basalts. *Contrib. Mineral. Petrol.* 166, 491–509. doi: 10.1007/s00410-013-0887-880
- Vona, A., Romano, C., Dingwell, D. B., and Giordano, D. (2011). The rheology of crystal-bearing basaltic magmas from Stromboli and Etna. *Geochim. Cosmochim. Acta* 75, 3214–3236. doi: 10.1016/j.gca.2011.03.031
- Wang, L., Liu, B., Li, H., Yang, W., Ding, Y., Sinogeikin, S. V., et al. (2012). Long-range ordered carbon clusters: a crystalline material with amorphous building blocks. *Science* 337:825. doi: 10.1126/science.1220522
- Weinberg, M. C., and Zanutto, E. (1989). Re-examination of the temperature dependence of the classical nucleation rate: homogeneous crystal nucleation in glass. *J. Non Cryst. Solids* 108, 99–108. doi: 10.1016/0022-3093(89)90337-2
- Xu, Y., Shankland, T. J., and Poe, B. T. (2000). Laboratory-based electrical conductivity in the Earth's mantle. *J. Geophys. Res.* 105, 895–827.
- Zanatta, M., Cormier, L., Hennes, L., Petrillo, C., and Sacchetti, F. (2017). Real-time observation of the isothermal crystallization kinetics in a deeply supercooled liquid. *Sci. Rep.* 7:43671. doi: 10.1038/srep43671
- Zhang, Y., Xu, Z., and Liu, Y. (2003). Viscosity of hydrous rhyolitic melts inferred from kinetic experiments, and a new viscosity model. *Am. Min.* 88, 1741–1752. doi: 10.2138/am-2003-11-1215
- Zheng, Q., Zhang, Y., Montazerian, M., Gulbiten, O., Mauro, J. C., Zanutto, E. D., et al. (2019). Understanding glass through differential scanning calorimetry. *Chem. Rev.* 119, 7848–7939. doi: 10.1021/acs.chemrev.8b00510
- Zieg, M. J., and Marsh, B. D. (2002). Crystal size distributions and scaling laws in the quantification of igneous texture. *J. Petrol.* 43, 85–101. doi: 10.1093/ptrology/43.1.85

Conflict of Interest: TH, MD, and AE were employed by the company Schott Glass North America.

The remaining authors declare that the research was conducted in the absence of any commercial or financial relationships that could be construed as a potential conflict of interest.

Copyright © 2020 Giuliani, Iezzi, Hippeli, Davis, Elbrecht, Vetere, Nazzari and Mollo. This is an open-access article distributed under the terms of the Creative Commons Attribution License (CC BY). The use, distribution or reproduction in other forums is permitted, provided the original author(s) and the copyright owner(s) are credited and that the original publication in this journal is cited, in accordance with accepted academic practice. No use, distribution or reproduction is permitted which does not comply with these terms.